ACS NANO

www.acsnano.org

ARTICLE

Following DNA Compaction During the Cell Cycle by X-ray Nanodiffraction

Clément Y. J. Hémonnot, Christiane Ranke, Oliva Saldanha, Rita Graceffa, Johannes Hagemann, and Sarah Köster*

Institute for X-ray Physics, University of Göttingen, Friedrich-Hund-Platz 1, Göttingen 37077, Germany

Supporting Information

ABSTRACT: **X-ray imaging of intact biological cells is emerging as a complementary method to visible light or electron microscopy. Owing to the high penetration depth and small wavelength of X-rays, it is possible to resolve subcellular structures at a resolution of a few nanometers. Here, we apply scanning X-ray nanodiffraction in combination with time-lapse bright-field microscopy to nuclei of 3T3 fibroblasts and thus relate the observed structures to specific phases in the cell division cycle. We scan the sample at a step size of 250 nm and analyze the individual diffraction patterns according to a generalized Porod's law. Thus, we obtain information on the aggregation state of the nuclear DNA at a real space resolution on the order of the step size and in parallel structural information on the order of few nanometers. We are able to distinguish nucleoli, heterochromatin, and euchromatin in the nuclei and follow the compaction and decompaction during the cell division cycle.**

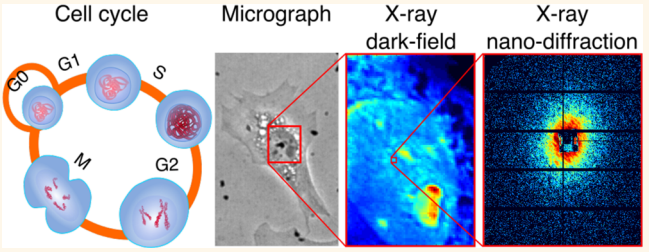

KEYWORDS: *nanostructure, X-ray nanodiffraction, biological cells, cell division cycle, DNA compaction*

Each nucleus in a mammalian cell contains 2 nm-thick DNA double helices[1] with a total length of about 2 m.[2,3] The DNA strands are packed in a highly hierarchical manner into individual chromosomes. During cell division, the DNA is unpacked, duplicated, and repacked, before copies of chromosomes are dragged into the two daughter cells such that each cell is equipped with a full set of chromosomes after division. The DNA double helix structure has been resolved by X-ray diffraction already in the 1950s,[1,4] and the existence of nucleosomes, 10 nm fibers, in which the double helices are wrapped around histone proteins like "beads-on-a-string",[5−8] has been shown in the 1970s. By contrast, less detail is known about the subsequent structure formation on length scales above 10 nm.[3] The 10 nm fibers are thought to fold into chromatin fibers with a diameter of 30 nm,[9,10] subsequently forming coiled structures of 300 nm diameter, coiled-coil complexes of 700 nm size, and finally chromosomes, which have a size of about 1 μm.[11,12] While the 30 nm chromatin fibers have been observed *in vitro*,[13,14] no clear evidence of such a structure has been reported *in vivo*, and its existence is still debated.[2,12,15] Within the cell nucleus, the DNA is not homogeneously distributed, but in regions of more or less densely packed DNA referred to as heterochromatin and euchromatin, respectively. Consequently, euchromatin is transcriptionally active by contrast to heterochramtin that is transcriptionally inactive due to the higher degree of condensation.[16] Moreover, inside the nucleus, these two structures are located at different specific regions: heterochromatin is found close to the nuclear envelope and around the nucleoli, whereas euchromatin is located more centrally.[7]

Thus, the length scales, on which DNA structure formation occurs in the nucleus, range between 2 nm and 1 μm. Consequently, besides direct imaging by electron microscopy (EM) with better and better resolution,[6,13,17] scattering by neutrons or X-ray photons has been widely employed to study the hierarchical structural levels. Early on, small angle neutron scattering (SANS) revealed the structure of chromatin particles with histones in the centers and DNA wrapped around[18] and small-angle X-ray scattering (SAXS) showed that the histones play an important role in maintaining the structural order in the chromatin.[19] Nishino *et al.* employed SAXS in combination with EM to show that the nucleosomes are irregularly arranged in the chromatin fibers.[20] Most early studies were performed on isolated *in vitro* systems, however, experiments on whole cells or isolated nuclei[21] also revealed the existence of a 30 nm structure which could correspond to chromatin fibers.

In recent years, novel X-ray techniques have been developed which combine the structural sensitivity of scattering methods with real space imaging. These imaging techniques complement EM and fluorescence microscopy by high resolution, due to a small wavelength, and high penetration power. Innovative

Received: July 27, 2016
Accepted: November 15, 2016
Published: November 15, 2016

DOI: 10.1021/acsnano.6b05034
ACS Nano 2016, 10, 10661−10670

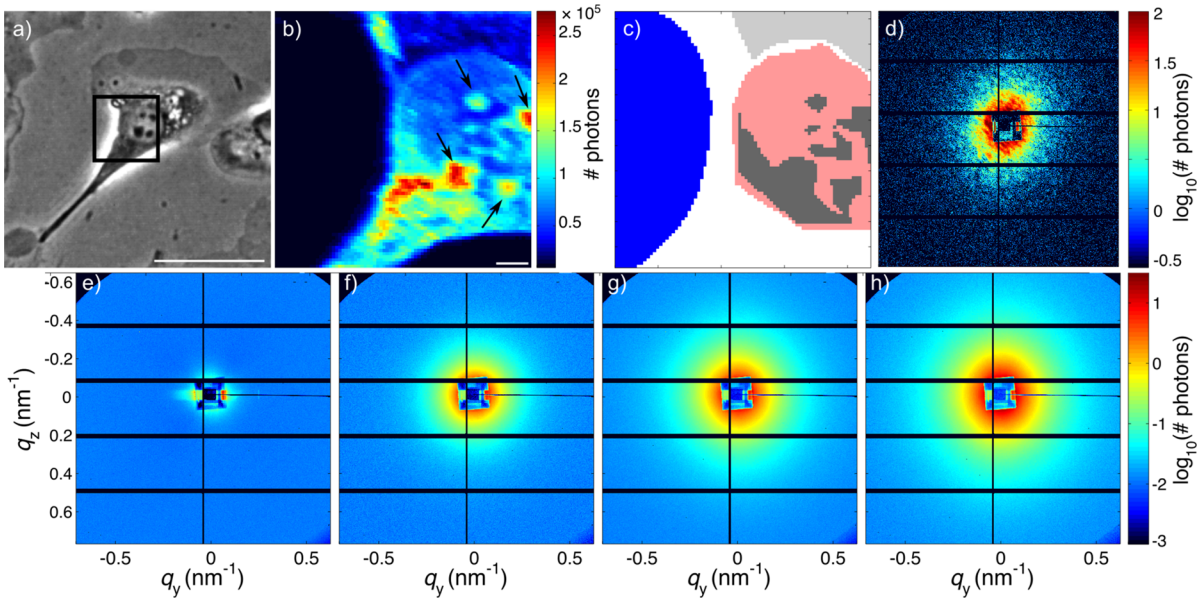

Figure 1. (a) Phase contrast image of a chemically fixed cell before freeze-drying. The black box indicates the ROI for the X-ray scan. The scale bar indicates 50 μm. (b) X-ray dark-field image of the ROI indicated in (a). The scale bar indicates 2.5 μm. (c) ROIs chosen for data analysis: background (blue), cytoplasm (light gray), euchromatin (red), and nucleoli/heterochromatin (dark gray). (d) Typical single diffraction pattern within the nuclear region. (e–h) Average signal (intensity *versus* scattering vector q) derived from the ROIs: (e) background, (f) cytoplasm, (g) euchromatin, and (h) nucleoli/heterochromatin.

developments in X-ray focusing optics[22,23] have led to beams focused down to the order of 100 nm that are now routinely available at specialized synchrotron facilities.[24−26] In the past, we and others have successfully employed scanning X-ray nanodiffraction on whole cells. Taking advantage of the nanofocused X-ray beam and thus avoiding spatial averaging as in standard X-ray scattering, these studies could resolve the local orientation and structure of the keratin networks in intact, unstained cells,[27−30] the order and orientation of actin filaments in hair cell stereocilia,[31] and the acto-myosin networks in *Dictyostelium discoideum* cells[32] and mesenchymal stem cells.[33] X-ray imaging has been applied to studying DNA packing in the nucleus in the past, in particular to *Deinococcus radiodurans* cells. By employing ptychography, the electron density was quantitatively measured[34,35] and extended to three dimensions by holography[36] and phase contrast tomography.[37] Coherent X-ray diffraction imaging in combination with visible light fluorescence microscopy was used to investigate nuclei of mammalian cells at a resolution of 20 nm, and the 3D architecture of nuclear substructures such as nucleolus and chromatin regions could be quantified.[38]

Thus, extremely valuable information was derived from studying DNA packing and compaction in the nucleus by X-ray imaging. An important drawback of the methods, however, remains that they are static, providing snap shots of certain stages during the cell division cycle. In order to understand the temporal evolution of the packing process, it is important to compare different stages. An interesting approach was taken by Spagnol *et al.* by chemically inducing DNA compaction and decompaction and quantifying the changes by fluorescence lifetime imaging microscopy (FLIM).[16]

Here, we employ X-ray nanodiffraction in combination with visible light phase contrast imaging on intact, freeze-dried fibroblasts to follow DNA compaction and decompaction during the different stages in the cell cycle. The correlative approach enables us to follow morphology and aggregation state of the DNA in a spatially and temporally resolved manner. We thus identify nuclear regions of particularly dense material as nucleoli and heterochromatin, surrounded by euchromatin, which is less densely packed. During the cell cycle, these nucleoli/heterochromatin regions are most strongly affected by DNA (de)compaction and changes in the size of scattering aggregates. Thus, we present results of a label-free technique to study important biological processes such as the DNA compaction and reorganization inside cells.

RESULTS AND DISCUSSION

Assessing Radiation Damage. It is possible to image hydrated and even (initially) living cells by scanning nanodiffraction,[28,29] but the electron density contrast between sample and environment is low, preventing sufficient photon statistics in the individual diffraction patterns. Moreover, in liquids, the motility of free radicals produced by water radiolysis[39] is very pronounced, leading to severe radiation damage.[39−41] Thus, in the past, we have mostly focused on freeze-dried samples providing a comparatively high electron density contrast and reducing the effect of radiation damage.[27,30,31] However, radiation damage still remains a challenge, and nanoscale defects caused by the radiation have to be carefully assessed. We have previously shown[29] that such nanoscale changes are observable in average diffraction patterns and in the related power law decay (Porod exponent). Thus, we compare different experimental settings for freeze-dried samples with a few recordings of cryoprotected samples. Cryoprotection has been shown to reduce the impact of ionizing radiation,[32,42] with the drawback of a more sophisticated and less versatile experimental setup that includes the cryostream. One has to be aware, however that both chemical fixation[29] and freeze-drying[43] of the cellular samples likely have an effect on intracellular nanostructure.

In total, we record the signal of 29 intact cells (26 freeze-dried and three in cryoprotected conditions). For each sample,

DOI: 10.1021/acsnano.6b05034
ACS Nano 2016, 10, 10661−10670

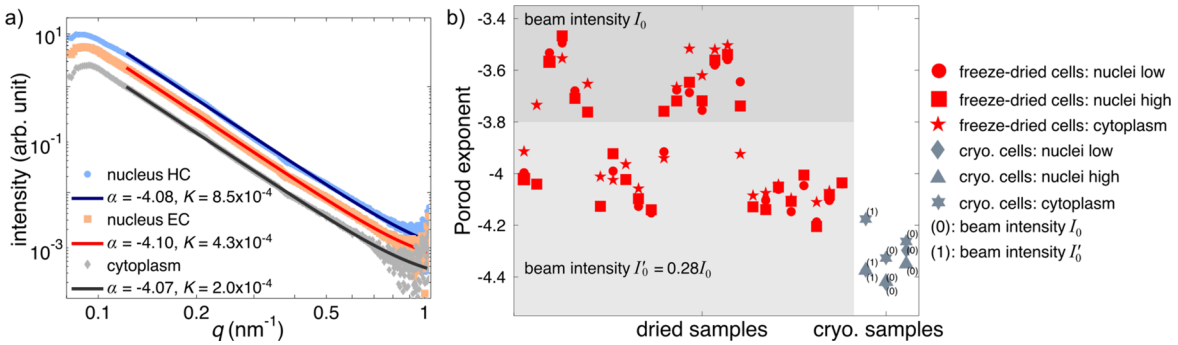

Figure 2. (a) Background corrected radial intensities corresponding to the ROIs shown in Figure 1 and fit by a generalized Porod's law (eq 2). More examples are shown in Figure S1 of the Supporting Information. (b) Porod exponents α of all investigated samples, *i.e.*, intact cells in freeze-dried and cryoprotected conditions. I_0 corresponds to the full beam and $I_0' = 0.28 \times I_0$ to the attenuated beam.

regions of interest (ROIs) are manually selected by carefully inspecting the visible light micrographs, and all diffraction patterns within these ROIs are averaged in order to obtain one 2D pattern for each ROI. An example of a typical scan is presented in Figure 1. Figure 1a shows a visible light phase contrast micrograph of the cell for comparison. In the X-ray dark-field image in Figure 1b, which identifies the total scattering in each scan point, different regions in the cell are identified as indicated by the colored ROIs in panel c. Within the nucleus we distinguish more strongly scattering regions (yellow to red on the color scale in Figure 1b) and less strongly scattering regions. The scattering power of a material is directly related to the electron density, number of scatterers, and their total volume (see eq 5 discussed further below). As the probed volume within the nucleus ($\sim 0.35 \times 0.43 \times 5\ \mu m^3$) is approximately constant from one scan point to another, the dark-field images provide a qualitative measure of the electron density.

In comparison to the visible light micrograph (Figure 1a), the globular high intensity regions (indicated by the black arrows in Figure 1b) can be assigned to nucleoli.[44,45] Note that additional strongly scattering material, which we assign to heterochromatin (HC), is not seen in the visible light micrograph. By contrast, we assign the less strongly scattering material to euchromatin (EC).[46−48]

The average signal for each of the four ROIs is shown in Figure 1e−h. Each of these average patterns is azimuthally integrated, and the 1D curves are background corrected by subtraction of the signal from the empty region (blue in Figure 1c). The radial intensity curves are plotted against the magnitude of the scattering vector:

$$q = \frac{4\pi}{\lambda} \sin\theta \tag{1}$$

with the X-ray wavelength λ and the scattering angle 2θ, as shown in Figure 2a. The curves are then fitted by a generalized Porod's law:[49]

$$I(q) = Kq^{\alpha} + B \tag{2}$$

to derive the Porod exponent $\alpha < 0$ and the Porod constant K. B is a constant that accounts for inelastic and incoherent scattering and small density fluctuations in the sample. The generalized Porod's law is not only valid for single particles but also for densely packed systems, as regarded in this study if we can assume a well-defined internal surface.[50] The Porod exponent α provides information about the morphology of the sample.[50,51] For an ideally thin rod, $\alpha = -1$, for a thin sheet, $\alpha = -2$, and for a spherical object with a smooth surface, $\alpha = -4$. Noninteger values are typical of mass fractals (α between -1 and -3) and surface fractals (α between -3 and -4).[52,53] As can be seen from the dark-field image, the heterochromatin and nucleoli scatter most strongly and the cytoplasm least strongly. We find similar exponents α for the three ROIs but very different values for K.

The exponents α of the investigated samples are shown in Figure 2b. For the freeze-dried samples (red symbols), two groups of data points can be identified, α close to -3.6 and α close to -4, which can almost unambiguously be assigned to data recorded with the full beam (I_0) and to data recorded with an attenuated beam ($I_0' = 0.28 \times I_0$), respectively. We have plotted the data in the temporal order in which we took them during the measurement campaign. Thus, for example, the first group of points (I_0') and the second group (I_0) stem from the same sample. We can thus exclude a mere influence of sample preparation on the exponents. Therefore, the difference in the exponent may be caused by radiation damage induced by the primary beam intensity. Better statistics by recording even more data sets would be needed to clearly prove this relationship between the beam intensity and the Porod exponent. Nonetheless, our hypothesis is supported by a direct comparison to data recorded from cryoprotected samples (gray symbols in Figure 2b). Here, we measure values for α around -4.3, independent of the attenuation. The different settings are marked by (0) for no attenuation, *i.e.*, a transmission of I_0 and (1) for a transmission of I_0', for each individual data point. In all experiments presented here, the exposure time is 100 ms, and the estimated dose[27] is calculated by approximating the cellular constituents with the empirical average chemical formula[54] $H_{50}C_{30}N_9O_{10}S$. Thus, the dose corresponds to about 2×10^8 Gy for the full beam and about 0.6×10^8 Gy with a transmission of $I_0' = 0.28 \times I_0$. We therefore conclude that with a beam attenuation by a factor of 3.6, the radiation damage is reduced almost to the level also reached by cryoprotection. A study on polysaccharide starch granules showed that the Porod exponent increases with the exposure time due to radiation damage,[55] which is in line with our results. As a consequence of this assessment, in the following we only consider recordings at an intensity of I_0' from 16 cells.

Temporal Evolution of DNA Nanostructure during the Cell Cycle. In order to relate the nuclear nanostructure to the different stages in the cell cycle, each cell needs to be analyzed according to previous divisions. Thus, we record time-lapse visible light bright-field microscopy movies (1 image every 5

DOI: 10.1021/acsnano.6b05034
ACS Nano 2016, 10, 10661−10670

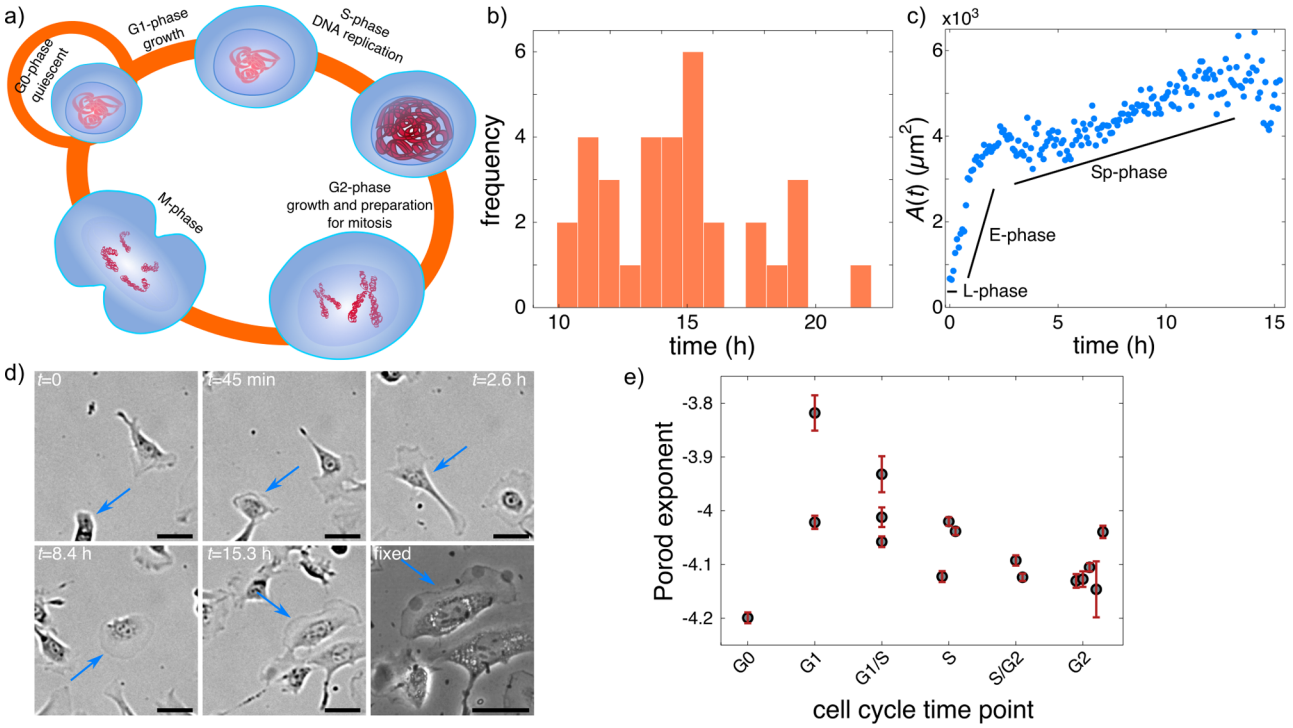

Figure 3. (a) Sketch of the different phases in the cell cycle. (b) Histogram of the cell cycle duration measured between two consecutive mitoses. (c) Area $A(t)$ of the cell marked in panel d plotted against time. Three growth phases are represented, the lag phase (L), the expansion phase (E), and the slow or steady spreading phase (Sp). (d) Snap-shot images of visible light phase contrast tracking of a cell over time. t = 0 corresponds to the time when the two daughter cells separate; the sample is chemically fixed after 15.3 h of time-lapse recording. Blue arrows mark the cell that is tracked. The scale bars indicate 50 μm. (e) Porod exponents from all 16 cells plotted against the cell cycle time points, error bars indicate the standard error derived from curve fitting.

min, duration 15−25 h) of the cells grown on silicon-rich nitride membranes. In Figure 3a, a sketch of the cell cycle is shown. During the gap 1 (G1) and gap 2 (G2) phase, cells and nuclei grow in volume,[2,56,57] and we observe an increase of the projected area. In between, during the synthesis (S) phase, the DNA is replicated.[58,59] During the mitosis (M) phase, cell division takes place. By analyzing the movies, we estimate the time between two consecutive divisions (M-phases) for 33 cells, as shown in the histogram in Figure 3b. We find an average cell cycle time length of 14.7 ± 3.0 h. Figure 3d shows individual movie frames at selected time points with the cell tracked in this example marked by the blue arrows.

Additionally, we extract the cell area and plot it against time as shown in Figure 3c. We define the time point t = 0 as the first movie frame where two daughter cells are distinguishable and track one of the daughter cells over time. The increase in cell area is characterized by three major phases: a lag phase (L), a fast expansion phase (E), and a slower spreading phase (Sp).[60] L-phase is regulated by complex actin filament assembly, and the cells are spherical.[61] In the E-phase the cells flatten and form thin disks.[61] It is characterized by a fast growth of the cell area. Subsequently, cell growth slow downs and finally reaches a plateau at the end of the Sp-phase, and the cell prepares for mitosis. Cell growth phases (L, E, Sp) and cell cycle phases (G1, S, G2, M) and in particular cell area growth and nuclear area growth are strongly correlated as shown, for example, for algae cells.[62]

Note that after identifying the influence of radiation damage on the Porod exponent, we here only consider cells recorded with an attenuated beam, thus average Porod exponents between −4.2 and −3.8. For our data analysis, we identify four groups of samples: (i) cells in the E-phase (corresponding to G1), (ii) cells in the early Sp-phase (corresponding to late G1 and early S), (iii) cells in the intermediate Sp-phase (corresponding to late S and early G2), and (iv) cells in the late Sp-phase (corresponding to G2). Note that in Figure 3e we include two additional subgroups (G1/S and S/G2) for cells that could not unambiguously be assigned to one group. For each cell, $A(t)$ is investigated in order to reveal the approximate stage of the cell in the cell cycle at the time point of fixation and subsequent X-ray measurement. For 16 samples, the Porod exponent of the whole nucleus is determined using eq 2. Figure 3e shows the data plotted against the estimated cell cycle time point. We observe an increase of the Porod exponent from G0 to G1. Subsequently α decreases along the cell cycle. These findings agree with our expectations: Cells in G0-phase are small, and thus the DNA is more compacted than for G1, when the cell and nucleus have grown. Indeed, as can be seen in Figure 3c, the cell area at the end of the E-phase is about 4 times larger compared to the area at t = 0. Subsequently, the size of the cells increases slowly, and the DNA content in the nucleus is doubled leading to a more compact state, in agreement with the decrease in the Porod exponent.[63,64] The fact that there is only a single cell scanned in G0 phase reflects the biological particularities of this stage: (i) this stage is very short and (ii) cells that have just divided have fewer adhesion points, hence these cells have a tendency to detach during the fixation and washing steps.

Spatially Resolved Analysis of DNA Nanostructure. We record a full diffraction pattern in each scan point (step size 250 nm × 250 nm). Therefore, in addition to the temporal evolution of DNA nanostructure during cell division as

DOI: 10.1021/acsnano.6b05034
ACS Nano 2016, 10, 10661−10670

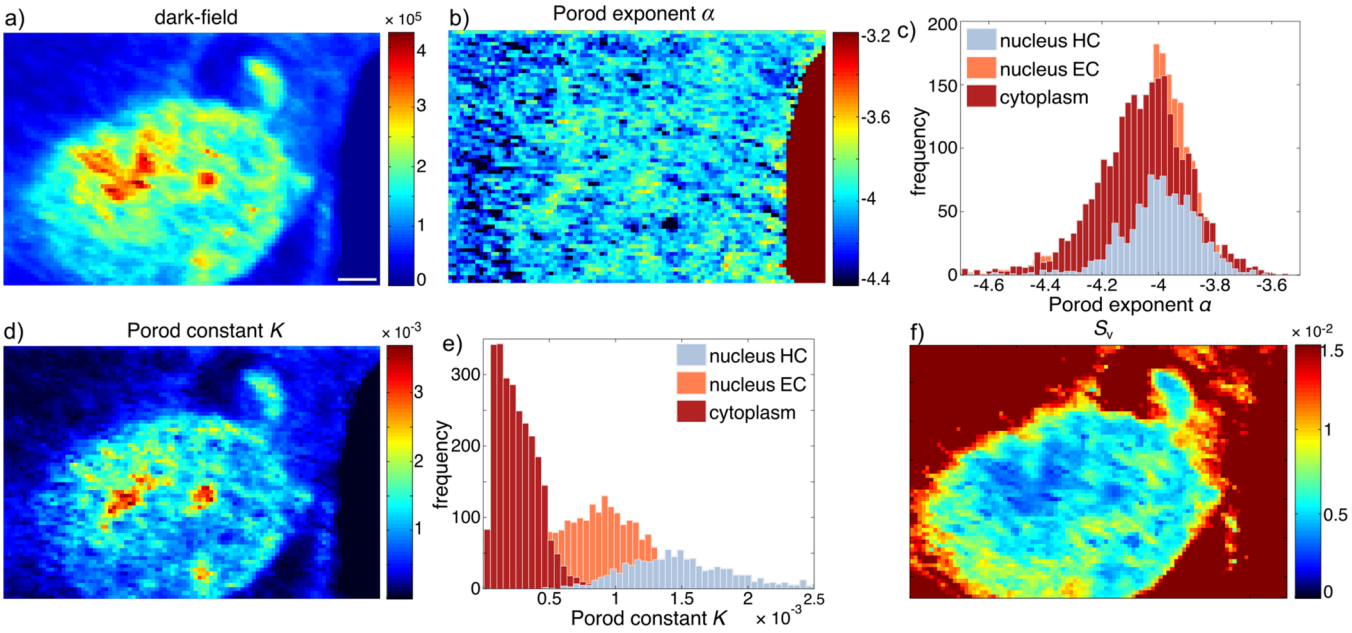

Figure 4. (a) Dark-field image of a cell; the color bar indicates the number of scattered photons. The scale bar indicates 2.5 μm. (b) Map of the Porod exponent α of the cell in (a) using a generalized Porod's law as described in eq 2 and (c) histogram of all individual Porod exponents from (b). (d) Map of the Porod constant K of the cell in (a) and (e) histogram of all individual Porod constants from (d). f) Map of the surface-area-to-volume ratio S_v (see Figure S2 in the Supporting Information for an example of another cell).

reported above, we have access to local information at a real space resolution of 350 × 430 nm^2. Figure 4 shows an example, where, as in Figure 1a,b, the cytoplasm as well as two nuclear regions (high intensity and low intensity in X-ray dark-field contrast) can be distinguished (panel a). Instead of averaging the patterns as above, we analyze each pattern individually according to eq 2. Both the Porod exponent α and the Porod constant K are plotted as maps in Figure 4b,d, respectively.

As stated above, the value of the Porod exponent α allows to retrieve the architecture of the sample. Experimentally, a value of −3.7 was found for DNA helices and −1.7 for DNA coils.[63] An exponent of −3.5 was reported corresponding to sponge-like structures.[65] We find Porod exponents between −3.8 and −4.2. Interestingly, the Porod exponent map shows that α is fairly homogeneously distributed within the investigated area (nucleus and cytoplasm) as shown in Figure 4b, and no pronounced differences between the different nuclear regions and between nucleus and cytoplasm are observed. Figure 4c shows histograms for each region (cytoplasm in red, nucleoli/heterochromatin in blue and euchromatin in orange) of the Porod exponents derived from the analysis of the individual cell shown in Figure 4. The distributions are fitted by Gaussian functions (see Figure S3 in the Supporting Information), revealing a mean on the order $\alpha = -4$ for all regions, whereas the standard deviation is slightly increased for the cytoplasm, indicating an increased structural heterogeneity as compared to the nucleus. Table 1 summarizes these results. As we found noninteger α values, typical of fractals or nonparticulate systems, other fit models such as the Beaucage model are commonly used for these systems.[66,67] This model has the advantage that it unifies the low q values (Guinier region) and the high q values (Porod region). Example fits of the Beaucage model are shown in Figure S4 in the Supporting Information. Both models (Porod and Beaucage) show good agreement with the experimental data. Here, we have focused on the Porod model because it provides an easier access to other SAXS parameters.

Table 1. Means and Standard Deviations of the Porod Exponent α and Constant K Distributions of Three ROIs within the Cell Shown in Figure 4

	ROI	mean	std
Porod exponent α	nucleus HC	−3.98	0.16
	nucleus EC	−3.99	0.15
	cytoplasm	−4.04	0.21
Porod constant K	nucleus HC	14.3×10^{-4}	5.5×10^{-4}
	nucleus EC	8.7×10^{-4}	5.1×10^{-4}
	cytoplasm	2.0×10^{-4}	2.6×10^{-4}

In addition to the Porod exponent, which has been widely analyzed for cell samples in the past,[29,32,33] eq 2 gives rise to the Porod constant K, shown in Figure 4d as a 2D map and in panel e as histograms. The spatial distribution resembles the dark-field image, with regions of higher and lower values in the nucleus. Table 1 shows distinctly different values for the three ROIs, where K is highest for the nucleoli/heterochromatin and lowest for regions located in the cytoplasm. In order to interpret the Porod constant K in a physical way, we recall that it is directly related to the specific surface or surface-area-to-volume ratio $S_v = SA_i/V_i$, where SA_i is the surface-area of object i and V_i is the volume of object i:[68,69]

$$K = 2\pi(\Delta\rho)^2 S_v \quad (3)$$

where $\Delta\rho$ is the excess scattering length density defined as $\Delta\rho = \rho_{sample} - \rho_{solvent}$. Here we have defined the Porod constant such that it is proportional to the number of scatterers N. S_v provides information about the compactness and the size of the probed objects. Larger values of S_v are expected for (i) smaller and (ii) less compact or aggregated objects. These two situations are schematically depicted in Figure 5c. As shown

DOI: 10.1021/acsnano.6b05034
ACS Nano 2016, 10, 10661−10670

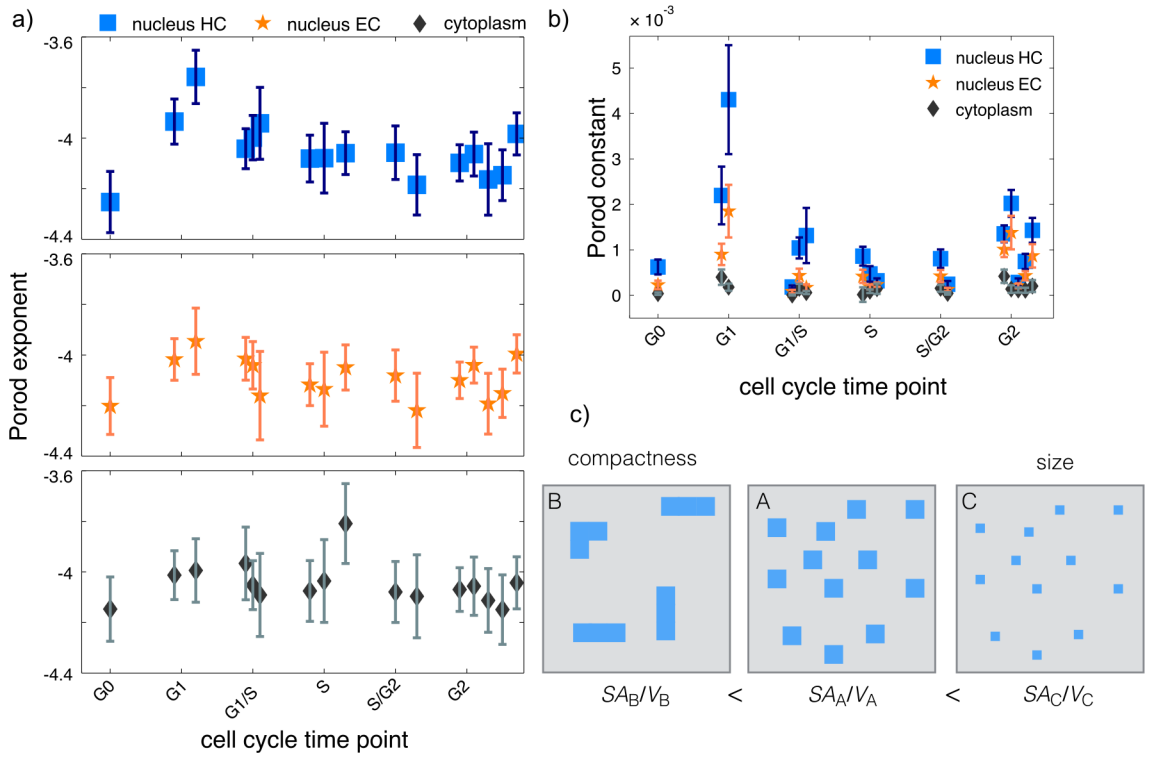

Figure 5. (a) Means and standard deviations of the distributions of Porod exponents α and (b) Porod constants K for the cells analyzed in Figure 3e, plotted separately for the three distinguished regions (nucleoli/heterochromatin as blue squares, euchromatin as orange stars, and cytoplasm as black diamonds). Each data point corresponds to one cell. (c) Schematic of the effect of aggregation (left) and structure size (right) on S_v: the sample is depicted in blue, the background in gray.

by eq 3, however, K is also directly related to the square of the electron density contrast of the sample. Thus, increased values of K either indicate higher electron density contrast, a higher number of particles, a less compact system, or smaller particle size.

From the dark-field images, $\Delta\rho$ is not quantitatively accessible. However, by the use of other SAXS quantities, it is possible to obtain an approximation of S_v. The Porod invariant Q is given by

$$Q = \int_0^\infty I(q)q^2 \mathrm{d}q = \frac{2\pi I_0}{V} \tag{4}$$

where I_0 is the zero angle (forward) scattering and V the volume of the scatterers. In any real experiment, the SAXS signal is only collected for q values between q_{min} and q_{max}. Thus, the values at low angles from 0 to q_{min} are determined by Guinier's approximation $Q_{Guinier} = \frac{I_0 q_{min}^3}{3}$ and the values at high angles between q_{max} to q_∞ are extrapolated using Porod's law leading to $Q_{Porod} = \frac{K}{q_{max}}$ (see Supporting Information for a detailed mathematical description).[70] On the other hand, the background corrected scattering intensity is defined as

$$I(q) = NV^2(\Delta\rho)^2 F(q)^2 \tilde{S}(q) \tag{5}$$

where N is the number of particles, and $F(q)$, and $\tilde{S}(q)$ are the form and structure factors, respectively, that is, the Fourier transforms of the shape and spatial arrangement of the system. In order to obtain an expression for S_v, we combine eqs 3, 4, and 5:

$$S_v \propto F(q)^2 \tilde{S}(q) {I_0}^2 \frac{K}{I(q)Q^2} \tag{6}$$

We can evaluate this expression in an approximative way from our data. The form factor $F(q)$, which describes the geometry of the scatters, is similar for all positions, as we found similar values of α values with a small standard deviation (0.16 for the nucleus of the cell shown in Table 1), indicating that the average probed structures at different positions have similar morphologies. Note that in this analysis, we refer to the spatial variation of the local structure from one scanning point to another, but for the same cell, *i.e.*, in the same cell cycle time point. By contrast, in the previous section we have shown that different cells have different α values during different time points in the cell cycle. The structure factor $\tilde{S}(q)$ can be neglected in the Porod regime (*i.e.*, at high q values $\tilde{S}(q) \simeq 1$);[50] this aspect is further supported by the fact we do not see features stemming from intraparticle structure. In order to take into account the scattering intensity at different q values, we define the dark-field signal as $I_{DF} = \sum_{q\in R} I(q)$, where R is the probed radial range.[71] Thus, we arrive at an approximation for the surface-area-to-volume ratio:

$$S_v = C\frac{K}{I_{DF}Q^2} \tag{7}$$

where C is a constant including I_0, $F(q)$, and $\tilde{S}(q)$ and accounting for the summation over all q. Note that because of the factors included in C, S_v is evaluated in arbitrary units.

Using this relation, we derive an approximated map of S_v from the maps of K and of I_{DF} for one cell (see the Supporting Information for another example of a different cell), as shown in Figure 4f. We observe regions of lower values that

DOI: 10.1021/acsnano.6b05034
ACS Nano 2016, 10, 10661−10670

correspond to the high intensity in the dark-field contrast, thus supporting the qualitative result from the dark-field images. It should be noted, however, that our approach presented here is only an approximation and other X-ray imaging methods may provide more precise information beyond the estimate we use here. By employing, for example, ptychography,[34,35] holography,[36] or phase contrast tomography,[37] $\Delta\rho$ may be directly accessed and used in eq 3. In our data, the nucleoli/heterochromatin regions show the lowest values of surface-area-to-volume ratio S_v, thus indicating an increased compactness and size of the probed scatterers. The euchromatin region still shows considerably larger, more compact scatterers than the cytoplasm. These results indicate a more aggregated, compacted state of the DNA found in the nucleoli/heterochromatin compared to the euchromatin. As expected, the cytoplasmic components, such as cytoskeletal proteins, are less aggregated. Note that this is not in contradiction to our discussion of the Porod exponent above; even though the morphology of the scatterers is mostly the same between the different ROIs, the degree of compaction is different.

In an effort to capture both the temporal evolution and the spatial variability of the DNA nanostructure, we plot the data of the different ROIs for 16 individual cells in Figure 5a,b in a cell cycle time point-dependent manner. Each symbol depicts the mean from all individually analyzed diffraction patterns within one ROI (nucleoli/heterochromatin, euchromatin, or cytoplasm, respectively) for one individual cell. The error bars denote the corresponding standard deviations. An increase in the Porod exponent during G1 phase is observed for the nuclear regions (blue squares and orange stars) but is almost negligible for the cytoplasm (black diamonds). This agrees with our expectations, as the cytoplasm and cytoskeletal constituents should not compact considerably during the cell cycle. For the 16 cells, we found an average standard deviation of 0.21, 0.21, and 0.27 for the nucleoli/heterochromatin, euchromatin, and cytoplasm, respectively. Thus, we observe an increased heterogeneity for the cytoplasm as compared to the nuclei, as expected.

The Porod constant (Figure 5b) provides information about the surface-area-to-volume ratio as well as the electron density contrast $\Delta\rho$. Our measurements show a strong increase for the nucleoli/heterochromatin regions, during G1 phase and to a lesser extent for the euchromatin, whereas the values from the cytoplasm are constant. Consistently, however, for all the 16 cells, K is highest in the high intensity parts of the nucleus and smallest for the cytoplasm.

CONCLUSIONS

Imaging biological samples at nanometer resolution while keeping them in a close-to-native state remains challenging. X-ray techniques such as scanning nanodiffraction offer the possibility to image intact, unsliced, and unstained cells at nanometer spatial resolution. By combining visible light microscopy time-lapse recordings with the nanodiffraction data, we additionally obtain access to the temporal evolution of the DNA compaction during the different cell cycle stages. After carefully assessing radiation damage, we use an imaging modality, which keeps the cellular nanostructure intact to a high degree. Individual X-ray diffraction patterns are recorded at a real space resolution of 350 × 430 nm^2, and we analyze data according to a generalized Porod's law (eq 2). Thus, we derive three independent quantities, the total scattering from the dark-field analysis, the Porod exponent α, which gives rise to structure morphology and compactness, and the Porod constant K, which provides a qualitative measure for the surface-area-to-volume ratio of the scatterers, thus providing information about the size and aggregation state of the probed biological material. Comparing the cell nucleus with the surrounding cytoplasm, we find an increased aggregation and material density, as shown by a stronger overall scattering in the dark-field images, a higher Porod constant, and a decreased surface-area-to-volume ratio. More specifically, we identify particularly dense and aggregated regions within the nucleus as the nucleoli and surrounding heterochromatin. Interestingly, the Porod exponent distribution within both nucleus and cytoplasm is not correlated with these distinguished regions. With regard to different cell cycle time points, between G0 and G1 phases, when the cell grows but the DNA is not doubled yet, we observe a pronounced decompaction of the DNA by an increase of the Porod exponents of the nuclei. Upon doubling of the DNA content, which occurs during S phase, the DNA compacts, and the Porod exponent decreases to its original value. Furthermore, we derive direct information about the aggregation state of the DNA in the nucleoli/heterochromatin and the euchromatin. Interestingly, the euchromatin is not very strongly affected during the cell cycle stages, as observed by only slight changes in the Porod constant. By contrast, however, the nucleoli/heterochromatin shows a strong increase for the Porod constant, in line with a decrease in size of probed aggregates during DNA decompaction. Thus, we present a method to study DNA compaction and decompaction during different time points in the cell cycle on intact cells and in a temporally and spatially resolved manner. Future experiments combining X-ray nanodiffraction with either a second imaging technique (*e.g.*, ptychography or holography) or live fluorescence microscopy, providing quantitative electron density contrast or information about cell cycle time points, respectively, will enable us to gain even more precise information on the nanostructure within cellular components. Given the rapid advancement of synchrotron sources, X-ray optics, and data analysis, it may even in the future become possible to identify stages in the cell cycle by SAXS measurements only avoiding the "detour" *via* optical microscopy.

MATERIALS AND METHODS

Cell Culture and Sample Preparation. We used 3T3 fibroblasts (NIH strain) from Swiss albino mouse embryos,[72] whose nuclei have a diameter of about 25 μm. The cells were grown in cell culture dishes in low glucose (1.0 g/L) Dulbecco's Modified Eagle Medium (DMEM), supplemented with L-glutamine and 10% (v/v) FCS, 100 units/mL penicillin, and 0.1 g/L streptomycin at 37 °C in a water-saturated atmosphere with 5% CO_2. When the cells reached about 80% confluence, they were detached from the culture dishes using 0.25% (v/v) trypsin and resuspended onto a fresh culture dish into which silicon-rich nitride membranes (frame size 5 × 5 mm^2, window size 1.5 × 1.5 mm^2, thickness 1 μm, Silson Ltd., Blisworth, England) had been placed. After 12 hours, the windows were placed in a stage-top incubation chamber, with identical culture conditions, and the incubation chamber was mounted on the sample stage of an inverted visible light microscope (IX81, Olympus, Hamburg, Germany). In order to obtain a large field of view, a 4× objective was employed, and bright-field images were recorded every 5 min for about 15 to 25 h. Afterward, the samples were washed with phosphate buffered saline (PBS), fixed with 3.7% formaldehyde solution supplemented with 1% methanol for 15 min, and washed three times for 5 min with PBS. Phase contrast microscopy images using 10× and 20× objectives were taken of each window. Samples were plunge-frozen and freeze-dried, as

DOI: 10.1021/acsnano.6b05034
ACS Nano 2016, 10, 10661−10670

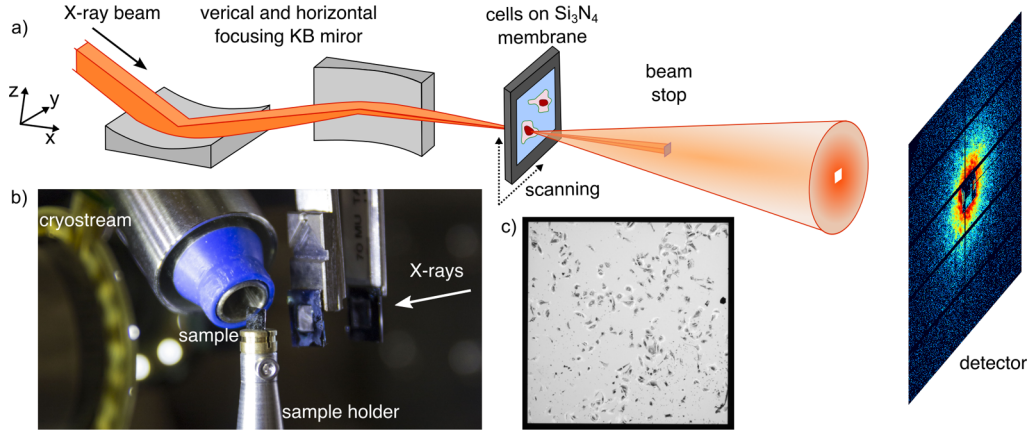

Figure 6. (a) Sketch of the setup. The X-ray beam points along the *x*-axis, and the sample is scanned through the beam in the *y*- and *z*-directions. (b) Photograph of the sample environment at the P10 beamline, PETRA III, DESY, Hamburg. (c) Bright-field image of freeze-dried cells on a silicon-rich nitride membrane (side length of the whole window is 1.5 mm).

described previously,[27,29,31−33] and inspected by bright-field and phase contrast microscopy at different stages of the sample preparation to identify possible artifacts from the preparation.

Scanning X-ray Nanodiffraction. We performed the X-ray nanodiffraction experiments at the coherence applications beamline P10 at the PETRAIII storage ring (DESY, Hamburg, Germany) and used the Göttingen Instrument for Nano Imaging with X-rays (GINIX).[73,74] The beam was delivered by a 5 m long undulator, directly followed by a cryo-cooled double crystal monochromator (Si-111) at an energy 8.0 keV. The beam was then focused by two Kirkpatrick−Baez (KB) mirrors (in cross geometry), as sketched in Figure 6a. The beam was focused to 350 × 430 nm^2 with a flux of 10^{11} photons/s and cleaned by apertures before reaching the sample. The sample was mounted on a piezoelectric stage allowing for fine translations down to 1 nm. The sample was aligned with an on-axis visible light microscope (reflectivity mode). Directly after the sample, a first beam stop (tungsten, 100 μm thickness, size 800 × 800 μm^2) was employed to block the primary beam. Subsequently, the scattered signal passed through a vacuum flight tube of 5 m length. The scattering signal was recorded using a single photon counting, high dynamic range Pilatus 300 K detector (487 × 619 pixels, pixel size: 172 × 172 μm^2; Dectris Ltd., Baden, Switzerland) or a Pilatus 1 M detector (981 × 1043 pixels, same pixel size as the 300 K), placed at the end of the flight tube. Due to the relatively high intensity of the beam, attenuators made out of aluminum were placed in front of the sample to reduce the beam intensity and to prevent severe radiation damage.

We first performed coarse scans of step size 2 × 2 μm^2 and exposure time of 50 ms to localize the cell. Subsequently, we performed fine scans on the nuclear region of the cell, with step sizes of 250 nm in both directions and an exposure time of 100 ms.

Data Analysis. The intensity recorded on the detector stems from the square modulus of the amplitude of the specimen's exit wave field, corresponding to the Fraunhofer far-field. In order to visualize the cell in real space, we computed X-ray dark-field images by integrating the full 2D diffraction patterns and plotting this integrated value at the position of the scan point. Furthermore, we analyzed the individual diffraction patterns. The 2D patterns were reduced to 1D radial intensity curves $I(q)$ by azimuthal integration. The curves were plotted against the scattering vector $q = \sqrt{{q_y}^2 + {q_z}^2}$ (eq 1). With our setup characteristics, we had access to a q-range of about [0.08, 1.04] nm^{-1}, thus accessing real space structures of about 6−80 nm. All diffraction patterns were corrected for exposure time and transmission of the filter used to reduce the primary beam intensity. Additionally, the beam current was used to normalize each scan point in order to account for variations of the beam intensity. The radial intensity curves were then fitted to a generalized Porod's law (eq 2). All the curves were fitted in the q range [0.12, 1.03] nm^{-1} by a nonlinear least-squares minimization.

ASSOCIATED CONTENT

Supporting Information

The Supporting Information is available free of charge on the ACS Publications website at DOI: 10.1021/acsnano.6b05034.

Additional $I(q)$ curves and fits with the Porod model; description of the surface-to-volume ratio; mathematical description of the Porod invariant calculation; and fits using the Beaucage model (PDF)

AUTHOR INFORMATION

Corresponding Author

*E-mail: sarah.koester@phys.uni-goettingen.de.

ORCID

Sarah Köster: 0000-0002-0009-1024

Notes

The authors declare no competing financial interest.

ACKNOWLEDGMENTS

The authors thank T. Salditt, M. Osterhoff, M. Priebe, and M. Sprung for fruitful discussions and technical assistance during the X-ray measurements and setting up the beam at the P10 coherence applications beamline, and S. Bauch and J. Herbst for providing technical assistance in cell culture and in sample preparation. This work was supported by the Helmholtz Gemeinschaft in the framework of Virtual Institute VH-VI-403 "*In Situ* Nano-Imaging of Biological and Chemical Processes", by the German Research Foundation (DFG) in the framework of SFB 755 "Nanoscale Photonic Imaging" within project C10, and by the German Ministry of Education and Research (BMBF) under grant no. 05K13OD4. Parts of this research were carried out at the light source PETRA III at DESY, a member of the Helmholtz Association (HGF).

REFERENCES

(1) Watson, J. D.; Crick, F. H. C. Molecular Structure of Nucleic Acids: A Structure for Deoxyribose Nucleic Acid. *Nature* **1953**, *171*, 737−738.

(2) Maeshima, K.; Hihara, S.; Eltsov, M. Chromatin Structure: Does the 30-nm Fiber Exist *in Vivo*? *Curr. Opin. Cell Biol.* **2010**, *22*, 291−297.

DOI: 10.1021/acsnano.6b05034
ACS Nano 2016, 10, 10661−10670

(3) Maeshima, K.; Imai, R.; Tamura, S.; Nozaki, T. Chromatin as Dynamic 10-nm Fibers. *Chromosoma* **2014**, *123*, 225−237.
(4) Franklin, R.; Gosling, R. Molecular Configuration in Sodium Thymonucleate. *Nature* **1953**, *171*, 740−741.
(5) Olins, A.; Olins, D. Spheroid Chromatin Units (v Bodies). *Science* **1974**, *183*, 330−332.
(6) Bednar, J.; Horowitz, R. A.; Grigoryev, S. A.; Carruthers, L. M.; Hansen, J. C.; Koster, A. J.; Woodcock, C. L. Nucleosomes, Linker DNA, and Higher Histone Form a Unique Structural Motif that Directs the Higher-Order Folding and Compaction of Chromatin. *Proc. Natl. Acad. Sci. U. S. A.* **1998**, *95*, 14173−14178.
(7) Olins, D. E.; Olins, A. L. Chromatin History: Our View From the Bridge. *Nat. Rev. Mol. Cell Biol.* **2003**, *4*, 809−814.
(8) Luger, K.; Dechassa, M. L.; Tremethick, D. J. New Insights Into Nucleosome and Chromatin Structure: An Ordered State or a Disordered Affair? *Nat. Rev. Mol. Cell Biol.* **2012**, *13*, 436−447.
(9) Robinson, P. J. J.; Rhodes, D. Structure of the '30 nm' Chromatin Fibre: A Key Role for the Linker Histone. *Curr. Opin. Struct. Biol.* **2006**, *16*, 336−343.
(10) Robinson, P. J. J.; Fairall, L.; Huynh, V. A. T.; Rhodes, D. EM Measurements Define the Dimensions of the "30-nm" Chromatin Fiber: Evidence for a Compact, Integrated Structure. *Proc. Natl. Acad. Sci. U. S. A.* **2006**, *103*, 6506−6511.
(11) Flors, C.; Earnshaw, W. C. Super-Resolution Fluorescence Microscopy as a Tool to Study the Nanoscale Organization of Chromosomes. *Curr. Opin. Chem. Biol.* **2011**, *15*, 838−844.
(12) Tremethick, D. J. Higher-Order Structures of Chromatin: The Elusive 30 nm Fiber. *Cell* **2007**, *128*, 651−654.
(13) Woodcock, C. L. F.; Safer, J. P.; Stanchfield, J. E. Structural Repeating Units in Chromatin. *Exp. Cell Res.* **1976**, *97*, 101−110.
(14) Chen, P.; Zhu, P.; Li, G. New Insights Into the Helical Structure of 30-nm Chromatin Fibers. *Protein Cell* **2014**, *5*, 489−491.
(15) Annunziatio, A. T. DNA Packing: Nucleosomes and Chromatin. *Nat. Educ.* **2015**, *1*, 1−26.
(16) Spagnol, S. T.; Dahl, K. N. Spatially Resolved Quantification of Chromatin Condensation Through Differential Local Rheology in Cell Nuclei Fluorescence Lifetime Imaging. *PLoS One* **2016**, *11*, e0146244.
(17) Song, F.; Chen, P.; Sun, D.; Wang, M.; Dong, L.; Liang, D.; Xu, R.-M.; Zhu, P.; Li, G. Cryo-EM Study of the Chromatin Fiber Reveals a Double Helix Twisted by Tetranucleosomal Units. *Science* **2014**, *344*, 376−380.
(18) Pardon, F. F.; Worcester, D. L.; Wooley, J. C.; Tatchell, K.; Van Holde, K. E.; Richards, B. M. Low-Angle Neutron Scattering from Chromatin Subunit Particles. *Nucleic Acids Res.* **1975**, *2*, 2163−2176.
(19) Fujiwara, S.; Inoko, Y.; Ueki, T. Synchrotron X-Ray Scattering Study of Chromatin Condensation Induced by Monovalent Salt: Analysis of the Small-Angle Scattering Data. *J. Biochem.* **1989**, *106*, 119−125.
(20) Nishino, Y.; Eltsov, M.; Joti, Y.; Ito, K.; Takata, H.; Takahashi, Y.; Hihara, S.; Frangakis, A. S.; Imamoto, N.; Ishikawa, T.; Maeshima, K. Human Mitotic Chromosomes Consist Predominantly of Irregularly Folded Nucleosome Fibres Without a 30-nm Chromatin Structure. *EMBO J.* **2012**, *31*, 1644−1653.
(21) Langmore, J. P.; Paulson, J. R. Low Angle X-Ray Diffraction Studies of Chromatin Structure in Vivo and in Isolated Nuclei and Metaphase Chromosomes. *J. Cell Biol.* **1983**, *96*, 1120−1131.
(22) Stangl, J.; Mocuta, C.; Chamard, V.; Carbone, D. *Nanobeam X-Ray Scattering*, 1st ed.; Wiley-VCH: Weinheim, Germany, 2014.
(23) Als-Nielsen, J.; McMorrow, D. *Elements of Modern X-Ray Physics*, 2nd ed.; John Wiley and Sons: Chichester, U.K., 2011.
(24) Schroer, C. G.; Kurapova, O.; Patommel, J.; Boye, P.; Feldkamp, J.; Lengeler, B.; Burghammer, M.; Riekel, C.; Vincze, L.; van der Hart, A.; Küchler, M. Hard X-Ray Nanoprobe Based on Refractive X-Ray Lenses. *Appl. Phys. Lett.* **2005**, *87*, 124103.
(25) Mimura, H.; Kimura, T.; Yokoyama, H.; Yumoto, H.; Matsuyama, S.; Tamasaku, K.; Koumura, Y.; Yabashi, M.; Ishikawa, T.; Yamauchi, K. Development of an Adaptive Optical System for Sub-10-nm Focusing of Synchrotron Radiation Hard X-Rays. *AIP Conf. Proc.* **2010**, *1365*, 13−17.
(26) Krüger, S. P.; Neubauer, H.; Bartels, M.; Kalbfleisch, S.; Giewekemeyer, K.; Wilbrandt, P. J.; Sprungc, M.; Salditt, T. Sub-10 nm Beam Confinement by X-Ray Waveguides: Design, Fabrication and Characterization of Optical Properties. *J. Synchrotron Radiat.* **2012**, *19*, 227−236.
(27) Weinhausen, B.; Nolting, J.-F.; Olendrowitz, C.; Langfahl-Klabes, J.; Reynolds, M.; Salditt, T.; Köster, S. X-Ray Nano-Diffraction on Cytoskeletal Networks. *New J. Phys.* **2012**, *14*, 085013.
(28) Weinhausen, B.; Köster, S. Microfluidic Devices for X-Ray Studies on Hydrated Cells. *Lab Chip* **2013**, *13*, 212−215.
(29) Weinhausen, B.; Saldanha, O.; Wilke, R.; Dammann, C.; Priebe, M.; Burghammer, M.; Sprung, M.; Köster, S. Scanning X-Ray Nanodiffraction on Living Eukaryotic Cells in Microfluidic Environments. *Phys. Rev. Lett.* **2014**, *112*, 088102.
(30) Hémonnot, C. Y. J.; Reinhardt, J.; Saldanha, O.; Patommel, J.; Graceffa, R.; Weinhausen, B.; Burghammer, M.; Schroer, C. G.; Köster, S. X-Rays Reveal the Internal Structure of Keratin Bundles in Whole Cells. *ACS Nano* **2016**, *10*, 3553−3561.
(31) Piazza, V.; Weinhausen, B.; Diaz, A.; Dammann, C.; Maurer, C.; Reynolds, M.; Burghammer, M.; Köster, S. Revealing the Structure of Stereociliary Actin by X-Ray Nanoimaging. *ACS Nano* **2014**, *8*, 12228−12237.
(32) Priebe, M.; Bernhardt, M.; Blum, C.; Tarantola, M.; Bodenschatz, E.; Salditt, T. Scanning X-Ray Nanodiffraction on *Dictyostelium Discoideum*. *Biophys. J.* **2014**, *107*, 2662−2673.
(33) Bernhardt, M.; Priebe, M.; Osterhoff, M.; Wollnik, C.; Diaz, A.; Salditt, T.; Rehfeldt, F. X-Ray Micro- and Nanodiffraction Imaging on Human Mesenchymal Stem Cells and Differentiated Cells. *Biophys. J.* **2016**, *110*, 680−690.
(34) Giewekemeyer, K.; Thibault, P.; Kalbfleisch, S.; Beerlink, A.; Kewish, C. M.; Dierolf, M.; Pfeiffer, F.; Salditt, T. Quantitative Biological Imaging by Ptychographic X-Ray Diffraction Microscopy. *Proc. Natl. Acad. Sci. U. S. A.* **2010**, *107*, 529−534.
(35) Wilke, R. N.; Priebe, M.; Bartels, M.; Giewekemeyer, K.; Diaz, A.; Karvinen, P.; Salditt, T. Hard X-Ray Imaging of Bacterial Cells: Nano-Diffraction and Ptychographic Reconstruction. *Opt. Express* **2012**, *20*, 19232−19254.
(36) Bartels, M.; Krenkel, M.; Haber, J.; Wilke, R. N.; Salditt, T. X-Ray Holographic Imaging of Hydrated Biological Cells in Solution. *Phys. Rev. Lett.* **2015**, *114*, 048103.
(37) Bartels, M.; Priebe, M.; Wilke, R. N.; Krüger, S. P.; Giewekemeyer, K.; Kalbfleisch, S.; Olendrowitz, C.; Sprung, M.; Salditt, T. Low-Dose Three-Dimensional Hard X-Ray Imaging of Bacterial Cells. *Optical Nanoscopy* **2012**, *1*, 10.
(38) Song, C.; Takagi, M.; Park, J.; Xu, R.; Gallagher-Jones, M.; Imamoto, N.; Ishikawa, T. Analytic 3D Imaging of Mammalian Nucleus at Nanoscale Using Coherent X-Rays and Optical Fluorescence Microscopy. *Biophys. J.* **2014**, *107*, 1074−1081.
(39) Riley, P. A. Free Radicals in Biology: Oxidative Stress and the Effects of Ionizing Radiation. *Int. J. Radiat. Biol.* **1994**, *65*, 27−33.
(40) Le Caër, S. Water Radiolysis: Influence of Oxide Surfaces on H2 Production Under Ionizing Radiation. *Water* **2011**, *3*, 235−253.
(41) Chapman, J. D.; Reuvers, A. P.; Borsa, J.; Greenstock, C. Chemical Radioprotection and Radiosensitization of Mammalian Cells Growing *in Vitro*. *Radiat. Res.* **2012**, *178*, AV214−AV222.
(42) Meisburger, S. P.; Warkentin, M.; Chen, H.; Hopkins, J. B.; Gillilan, R. E.; Pollack, L.; Thorne, R. E. Breaking the Radiation Damage Limit with Cryo-SAXS. *Biophys. J.* **2013**, *104*, 227−236.
(43) Casanova, G.; Nolin, F.; Wortham, L.; Ploton, D.; Banchet, V.; Michel, J. Shrinkage of Freeze-Dried Cryosections of Cells: Investigations by EFTEM and Cryo-CLEM. *Micron* **2016**, *88*, 77−83.
(44) Lo, S. J.; Lee, C.-C.; Lai, H.-J. The Nucleolus: Reviewing Oldies to Have New Undestandings. *Cell Res.* **2006**, *16*, 530−538.
(45) Pederson, T. The Nucleolus. *Cold Spring Harbor Perspect. Biol.* **2011**, *3*, a000638.
(46) Anastrassova-Kristeva, M. The Nucleolar Cycle in Man. *J. Cell Sci.* **1977**, *25*, 103−110.
(47) Tsai, R. Y. L.; Pederson, T. Connecting the Nucleolus to the Cell Cycle and Human Disease. *FASEB J.* **2014**, *28*, 3290−3296.

DOI: 10.1021/acsnano.6b05034
ACS Nano 2016, 10, 10661−10670

(48) Padeken, J.; Heun, P. Nucleolus and Nuclear Periphery: Velcro for Heterochromatin. *Curr. Opin. Cell Biol.* **2014**, *28*, 54−60.
(49) Porod, G. Die Röntgenkleinwinkelstreuung von dichtgepackten Kolloiden Systemen. *Colloid Polym. Sci.* **1951**, *124*, 83−114.
(50) Glatter, O.; Kratky, O. *Small Angle X-Ray Scattering*; Academic Press: New York, 1982.
(51) Guinier, A.; Fournet, G. *Small-Angle Scattering of X-Rays*; John Wiley and Sons: New York, 1955.
(52) Teixeira, J. Small-Angle Scattering by Fractal Systems. *J. Appl. Crystallogr.* **1988**, *21*, 781−785.
(53) Beaucage, G. Small-Angle Scattering from Polymeric Mass Fractals of Arbitrary Mass-Fractal Dimension. *J. Appl. Crystallogr.* **1996**, *29*, 134−146.
(54) Howells, M. R.; Beetz, T.; Chapman, H. N.; Cui, C.; Holton, J. M.; Jacobsen, C. J.; Kirz, J.; Lima, E.; Marchesini, S.; Miao, H.; Sayre, D.; Shapiro, D. A.; Spence, J. C. H.; Starodub, D. An Assessment of the Resolution Limitation Due to Radiation-Damage in X-Ray Diffraction Microscopy. *J. Electron Spectrosc. Relat. Phenom.* **2009**, *170*, 4−12.
(55) Cojoc, D.; Amenitsch, H.; Ferrari, E.; Santucci, S. C.; Sartori, B.; Rappolt, M.; Marmiroli, B.; Burghammer, M.; Riekel, C. Local X-Ray Structure Analysis of Optically Manipulated Biological Micro-Objects. *Appl. Phys. Lett.* **2010**, *97*, 244101.
(56) Fidorra, J.; Mielke, T.; Booz, J.; Feinendegen, L. E. Cellular and Nuclear Volume of Human Cells During the Cell Cycle. *Radiat. Environ. Biophys.* **1981**, *19*, 205−214.
(57) Huber, M. D.; Gerace, L. The Size-Wise Nucleus: Nuclear Volume Control in Eukaryotes. *J. Cell Biol.* **2007**, *179*, 583−584.
(58) Pardee, A. B. G1 Events and Regulation of Cell Proliferation. *Science* **1989**, *246*, 603−608.
(59) Alberts, B.; Johnson, A.; Lewis, J.; Raff, M.; Roberts, K.; Walter, P. *Molecular Biology of the Cell*, 4th ed.; Garland Science: New York, 2002.
(60) Huang, C.-H.; Donald, A. Revealing the Dependence of Cell Spreading Kinetics on its Spreading Morphology Using Microcontact Printed Fibronectin Patterns. *J. R. Soc., Interface* **2015**, *12*, 20141064.
(61) Döbereiner, H.-G.; Dujardin-Thaler, B. J.; Ciannone, G.; Sheetz, M. P. Force Sensing and Generation in Cell Phases: Analyses of Complex Functions. *J. Appl. Physiol.* **2005**, *98*, 1542−1546.
(62) Dapena, C.; Bravo, I.; Cuadrado, A.; Figueroa, R. I. Nuclear and Cell Morphological Changes During the Cell Cycle and Growth of the Toxic Dinoflagellate *Alexandrium minutum*. *Protist* **2015**, *166*, 146−160.
(63) Hammouda, B.; Worcester, D. The Denaturation Transition of DNA in Mixed Solvents. *Biophys. J.* **2006**, *91*, 2237−2242.
(64) Hammouda, B. *Probing Nanoscale Structures - The SANS Toolbox*; National Institute of Standards and Technology: Gaithersburg, MD, 2010.
(65) Ho, D.; Hammouda, B.; Kline, S. R.; Chen, W.-R. Unusual Phase Behavior in Mixtures of Poly Ethylene Oxide and Ethyl Alcohol. *J. Polym. Sci., Part B: Polym. Phys.* **2006**, *44*, 557−564.
(66) Beaucage, G. Approximations Leading to a Unified Exponential/Power-Law Approach to Small-Angle Scattering. *J. Appl. Crystallogr.* **1995**, *28*, 717−728.
(67) Hammouda, B. Analysis of the Beaucage Model. *J. Appl. Crystallogr.* **2010**, *43*, 1474−1478.
(68) Fratzl, P.; Fratzl-Zelman, N.; Klaushofer, K.; Vogl, G.; Koller, K. Nucleation and Growth of Mineral Crystals in Bone Studied by Small-Angle X-Ray Scattering. *Calcif. Tissue Int.* **1991**, *48*, 407−413.
(69) Fratzl, P.; Schreiber, S.; Klaushofer, K. Bone Mineralization as Studied by Small-Angle X-Ray Scattering. *Connect. Tissue Res.* **1996**, *34*, 247−254.
(70) Gourrier, A.; Li, C.; Siegel, S.; Paris, O.; Roschger, P.; Klaushofer, K.; Fratzl, P. Scanning Small-Angle X-Ray Scattering Analysis of the Size and Organization of the Mineral Nanoparticles in Fluorotic Bone Using a Stack of Cards Model. *J. Appl. Crystallogr.* **2010**, *43*, 1385−1392.
(71) Bunk, O.; Bech, M.; Jensen, T. H.; Feidenhans'l, R.; Binderup, T.; Menzel, A.; Pfeiffer, F. Multimodal X-Ray Scatter Imaging. *New J. Phys.* **2009**, *11*, 123016.
(72) Todaro, G. J.; Green, H. Quantitative Studies of the Growth of Mouse Embryo Cells in Culture and their Development into Established Lines. *J. Cell Biol.* **1963**, *17*, 299−313.
(73) Kalbfleisch, S.; Osterhoff, M.; Giewekemeyer, K.; Neubauer, H.; Krüger, S. P.; Hartmann, B.; Bartels, M.; Sprung, M.; Leupold, O.; Siewert, F.; Salditt, T. The Holography Endstation of Beamline P10 at PETRA III. *AIP Conf. Proc.* **2009**, *1234*, 433−436.
(74) Salditt, T.; Osterhoff, M.; Krenkel, M.; Wilke, R. N.; Priebe, M.; Bartels, M.; Kalbfleisch, S.; Sprung, M. Compound Focusing Mirror and X-Ray Waveguide Optics for Coherent Imaging and Nano-Diffraction. *J. Synchrotron Radiat.* **2015**, *22*, 867−878.

DOI: 10.1021/acsnano.6b05034
ACS Nano 2016, 10, 10661−10670